communications physics

Article

https://doi.org/10.1038/s42005-024-01784-6

Non-equilibrium formation and relaxation of magnetic flux ropes at kinetic scales

Check for updates

Young Dae Yoon [1,2] ✉, **Modhuchandra Laishram** [1], **Thomas Earle Moore** [3] & **Gunsu S. Yun** [2,4]

Magnetic flux ropes are pivotal structures and building blocks in astrophysical and laboratory plasmas, and various equilibrium models have thus been studied in the past. However, flux ropes in general form at non-equilibrium, and their pathway from formation to relaxation is a crucial process that determines their eventual properties. Here we show that any localized current parallel to a background magnetic field will evolve into a flux rope via non-equilibrium processes. The detailed kinetic dynamics are exhaustively explained through single-particle and Vlasov analyses and verified through particle-in-cell simulations. This process is consistent with many proposed mechanisms of flux rope generation such as magnetic reconnection. A spacecraft observation of an example flux rope is also presented; by invoking the non-equilibrium process, its structure and properties can be explicated down to all six components of the temperature tensor.

Magnetic flux ropes are twisted bundles of magnetic field lines that confine current-carrying plasma and are fundamental and ubiquitous structures in space, astrophysical, and laboratory plasmas[1–14]. They act as underlying structures in various plasma phenomena and instabilities, serving as magnetic batteries that convert magnetic energy into other forms of energy via processes such as magnetic reconnection[6,15], eruption[7,8,16], flux transfer events (FTEs)[17], and current-driven/kinetic instabilities[18,19]. Due to their significance, various equilibrium models such as force-free models[20–22], magnetohydrodynamic (MHD) models[5], and MHD models including deformation effects[23–25] have been developed to explain various observed characteristics of these structures.

Despite extensive studies, no single model can comprehensively interpret flux ropes. For example, only 60% of flux ropes observed in the magnetotail can be described by force-free models[4]. Also, many small-scale flux ropes admit anisotropic/off-diagonal pressure tensor components[26], which MHD models and widely-used Grad–Shafranov reconstruction methods cannot accommodate. Thus, there is a need to revisit the problem of whether all flux ropes are alike in terms of morphology, magnetic and plasma properties, and dynamics, and answering this question calls for a revelation of their formation, relaxation, and evolution[27]. In particular, for (sub-)ion-scale systems, the detailed structure of the particle distribution function is an important determining factor of their stability and subsequent dynamics.

Now, recent investigations[28,29] of collisionless current sheet relaxation revealed the process through which a current sheet that has formed at non-equilibrium undergoes relaxation to a final equilibrium. It was shown that non-equilibrium dynamics must be taken into account to explain the eventual structure of the equilibrium; notably, the origin of bifurcated structures was readily explained by invoking said non-equilibrium dynamics. Also, how a particular equilibrium is selected from an infinite number of possibilities was explained. It was also shown that detailed dynamics of the particle distribution function in phase-space is crucial for the explication of the structures.

Because flux ropes are cylindrical cousins of Cartesian current sheets, it is also expected that non-equilibrium dynamics and detailed phase-space distributions must be invoked to construct correct flux rope models. Although flux ropes in general should form at non-equilibrium states, the pathway from initial to final states has been relatively less understood. For instance, although most laboratory experiments initially induce only parallel current density to generate flux ropes, the eventual current density develops a twist[7,18].

Here we present an analysis of the non-equilibrium formation and relaxation process of a flux rope at kinetic scales. The process is thoroughly understood using collective phase-space analysis. It is shown by considering pinching dynamics that a localized current flowing parallel to a magnetic field is a sufficient condition for the formation of a flux rope. This process is consistent with many proposed mechanisms of flux rope generation such as magnetic reconnection. Our investigation attributes the observed structural characteristics of a representative flux rope observed in space exclusively to these kinetic dynamics, thereby encompassing all six components of the electron temperature tensor.

Results

Formation process

Consider the following model distribution function, magnetic field, and current density profiles for a current-carrying flux tube along a uniform

---

[1]Asia Pacific Center for Theoretical Physics, Pohang, Gyeongbuk, 37673, South Korea. [2]Department of Physics, Pohang University of Science and Technology, Pohang, Gyeongbuk, 37673, South Korea. [3]3rd Rock Research, Annapolis, MD, 21401, USA. [4]Department of Advanced Nuclear Engineering, Pohang University of Science and Technology, Pohang, Gyeongbuk, 37673, South Korea. ✉e-mail: youngdae.yoon@apctp.org

guide field in cylindrical coordinates:

$$f_\sigma(r,\mathbf{v}) = \left(\frac{1}{2\pi v_{T\sigma}^2}\right)^{3/2} \exp\left(-\frac{(\mathbf{v}-V_\sigma\hat{z})^2}{2v_{T\sigma}^2}\right)\frac{n_0}{\left(1+r^2/\lambda^2\right)^2}, \quad (1)$$

$$\mathbf{B}(r) = \hat{\phi}\frac{B_0 r/\lambda}{1+r^2/\lambda^2} + \hat{z} b_g B_0, \quad (2)$$

$$\mathbf{J}(r) = \hat{z}\frac{B_0}{\mu_0\lambda}\frac{2}{\left(1+r^2/\lambda^2\right)^2}, \quad (3)$$

and the electrostatic potential $\Phi = 0$, where the subscript $\sigma = i, e$ is for the ion and electron species, $v_{T\sigma}$ and V_σ are the species thermal and drift velocities, n_0 and B_0 are the reference density and magnetic field, λ is the radial tube thickness, and b_g is the relative guide field strength. This is in fact the Bennett solution[30] under a guide field but the drift and thermal velocities are left arbitrary so that it is not necessarily an equilibrium solution. The initial parallel current is assumed to have been induced by a parallel electric field whose source may arise from, e.g., guide-field reconnection, kinetic instabilities, turbulence, or boundary sources[8,9,19,31–35]. Note that ideal MHD cannot support parallel electric fields due to Ohm's law, hinting the need for non-ideal-MHD mechanisms. Also note that there are other methods such as electron cyclotron current drive (ECCD) in fusion contexts that can also drive parallel current and form flux ropes as well[36].

Now we define $\bar{r} = r/\lambda$, $\bar{t} = q_\sigma B_0 t/m_\sigma = \omega_{c\sigma} t$ where q_σ and m_σ are the charge and mass of each species, $\bar{v} = v/\lambda\omega_{c\sigma}$ for any velocity v, and normalize the magnetic field by B_0, and density by n_0. Inserting Eqs. (1) and (2) into the Vlasov equation yields:

$$\frac{\partial \ln f_\sigma}{\partial \bar{t}} = -\bar{v}_r\frac{4\bar{r}}{1+\bar{r}^2}\left(\frac{\bar{V}_\sigma}{4\bar{v}_{T\sigma}^2}-1\right). \quad (4)$$

Denoting $\xi = \bar{V}_\sigma/4\bar{v}_{T\sigma}^2 - 1$, $\xi = 0$ corresponds to the Bennett equilibrium[30]. Because V_σ is associated with current density and $v_{T\sigma}$ with thermal pressure, ξ measures the balance between the radially-inward pinching force and the outward thermal force. Note that if the radial dependence of f_σ is eliminated and $b_g = \left(1+\bar{r}^2\right)^{-1}$, the system corresponds to the Gold-Hoyle flux tube[20], where the inward pinching force is balanced by a gradient in the guide field.

If $\xi \neq 0$, Eq. (4) yields a solution after a small linear time interval $\delta\bar{t}$ (discarding $\mathcal{O}\left(\delta\bar{t}^2\right)$):

$$f_\sigma \sim \exp\left(-\frac{\left(\bar{\mathbf{v}}-\bar{V}_\sigma\hat{z}-\bar{V}_{r\sigma}\hat{r}\right)^2}{2\bar{v}_{T\sigma}^2}\right), \quad (5)$$

where

$$\bar{V}_{r\sigma} = -4\bar{v}_{T\sigma}^2\xi\delta\bar{t}\frac{\bar{r}}{1+\bar{r}^2}, \quad (6)$$

which shows that if $\xi > 0$, there is a radial focusing of f_σ towards $r = 0$, i.e., pinching. This radial velocity couples to B_z, generating an azimuthal velocity which in turn creates an azimuthal current; this is equivalent to the plasma carrying the guide field towards the center and effectively amplifying it.

The preceding analysis prompts the following model for the non-equilibrium formation of a flux rope, as shown in Fig. 1. Consider a radially localized current parallel to a seed (not necessarily small) guide magnetic field, embedded in a plasma whose thermal pressure cannot balance the pinching force, e.g., a uniform plasma. The current density will then pinch, focusing and magnifying both the plasma density and the guide magnetic field near $r = 0$ until an equilibrium is reached. The guide magnetic field becomes peaked near $r = 0$, corresponding to a finite azimuthal current (red arrowed circle). The final equilibrium is thus a flux rope involving twisted magnetic field lines, twisted current density, and central plasma confinement, and it can be thought of as a mixture of the Bennett and Gold-Hoyle flux tubes[20,30], where the pinching force is balanced by a combination of gradients in the thermal pressure and the axial field. The detailed profile of the final equilibrium may vary greatly and depends entirely on the initial conditions at which the initial parallel current was induced. For example, the higher the initial plasma beta, the less pinching the flux rope will experience due to the higher expansive force. Or, if the initial guide field is non-existent, there will be no azimuthal current because there is no guide-field amplification.

Numerical results

To corroborate and study the above process in detail, 2D particle-in-cell (PIC) simulations were conducted in Cartesian geometry, i.e., $r = \sqrt{x^2+y^2}$. The initial conditions of the fiducial run were Eqs. (1) and (2), with $\lambda = 2d_i$ where d_i is the collisionless ion skin depth, $b_g = 0.15$, and $4\bar{v}_{T\sigma}^2 = 0.2\bar{V}_\sigma$ so $\xi = 4$. A reduced mass ratio of $m_i/m_e = 100$ was used, and the Alfvén velocity $v_A/c = 0.1$. The system reaches equilibrium at around $100\omega_{pi}^{-1}$. The resultant 2D data were repeated in the z-direction to generate 3D data.

Figure 2 shows initial (a and c) and final (b and d) states of **B**, the current density **J** and the thermal pressure P, calculated with the trace of the ion and electron pressure tensors, namely $\mathrm{Tr}\left(\mathbf{P}_i+\mathbf{P}_e\right)/3$. The quantities are in units of B_0, $n_0 e v_A$, and $n_0 m_i v_A^2$, respectively. Initially, **J** is purely in the axial direction, and **B** is mainly azimuthal with a relatively small axial component. After pinching, **J** is enhanced and also importantly develops an azimuthal component, i.e., becomes twisted. The twisting of **J** corresponds to a local amplification of the background guide field by a factor of 4, resulting in a decrease of the magnetic field pitch angle with respect to $\hat{z}$. P is also locally amplified by a factor of 8 (the initial peak pressure is around

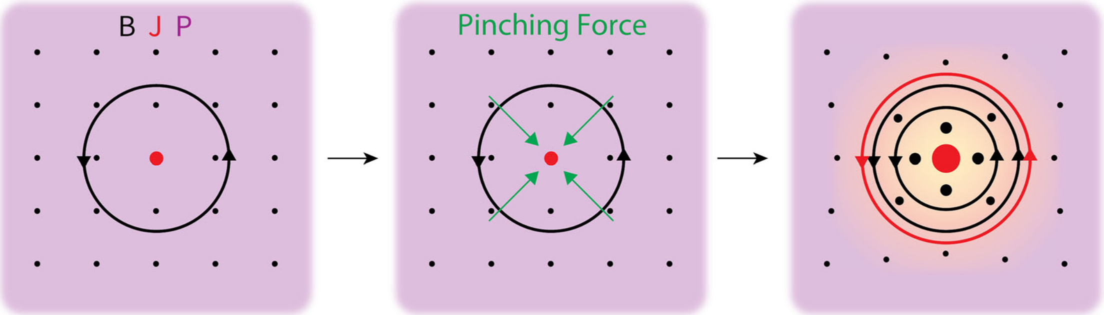

Fig. 1 | Formation process of a flux rope. In a plasma with a uniform pressure P (pink color), a localized current **J** (red dots) parallel to the guide magnetic field **B** (black dots) induces an azimuthal magnetic field (black arrowed circles). The current pinches due to the pinching force (green arrows) and amplifies, carrying the guide field and plasma pressure towards the center and amplifying them. Guide field amplification corresponds to azimuthal current generation (red arrowed circle).

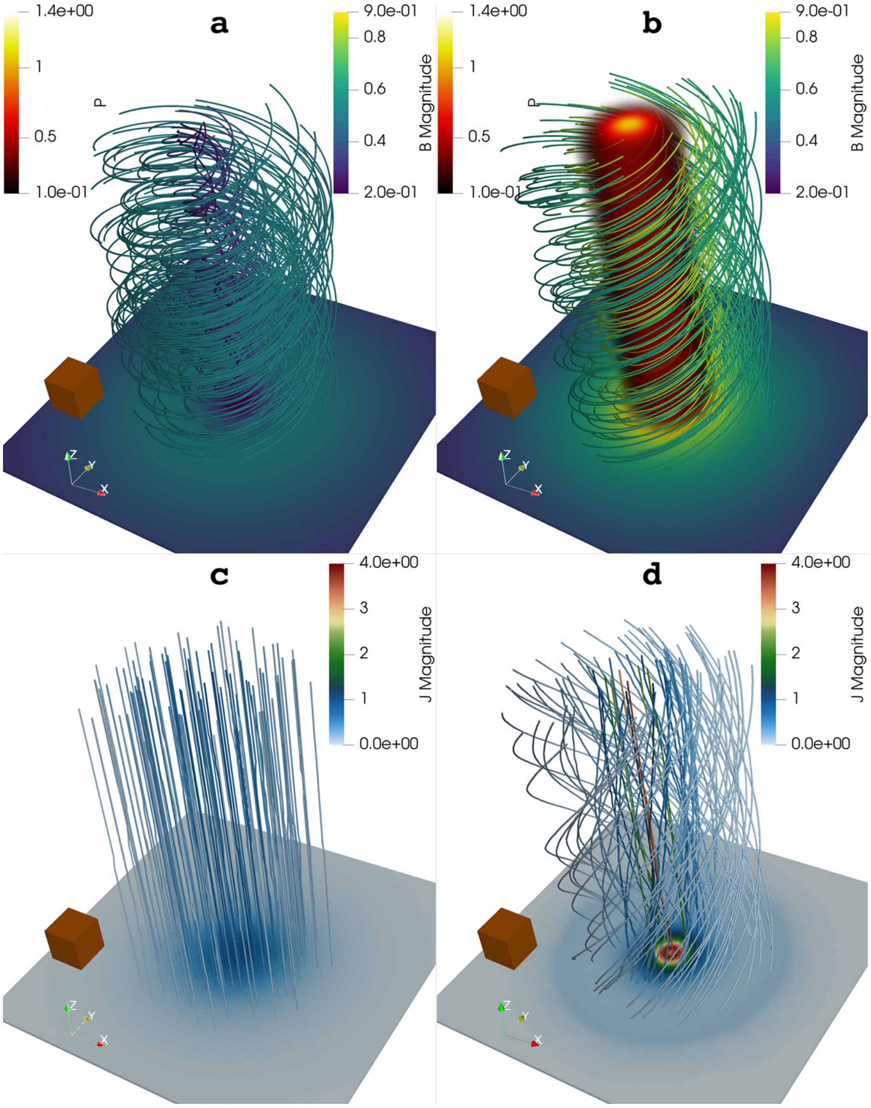

Fig. 2 | Initial and final states from the PIC simulation. The magnetic field **B** and the plasma pressure P at **a** $t = 0$ and **b** $t = 200\omega_{\mathrm{pi}}^{-1}$, in units of B_0 and $n_0 m_i v_A^2$, respectively. The current density **J** at **c** $t = 0$ and **d** $t = 200\omega_{\mathrm{pi}}^{-1}$ in units of $n_0 e v_A$. The total dimension is $(x, y, z) = (10, 10, 10)d_i$, and brown cubes of side lengths of $1d_i$ are also plotted for scale reference.

0.17), indicating plasma confinement. It is clear from the final states that a flux rope has been generated simply by a localized parallel current trying to reach equilibrium.

Figure 3a–f shows the initial (a–c) and final (d–f) 2D profiles of **B, J**, and P corresponding to those in Fig. 2. The amplification of B_z, generation of J_ϕ, and confinement of P are evident. Figure 3g–l are all six elements of the electron pressure tensor, which are determined by the possible particle trajectories in phase-space, as will be seen shortly. A seemingly unexpected development is the negative J_ϕ (black lines in Fig. 3e), as opposed to the positive J_ϕ at the outskirts (white lines in Fig. 3e), that induces a central dip in B_z (color in Fig. 3d). This is a finite Larmor radius effect where the axis-encircling particles undergo diamagnetic acceleration. Another feature is the ring-like structure of J_z and P_{ezz} (Fig. 3e, i), which is due to conservation of canonical momentum as will be seen later.

Single-particle and kinetic analysis

Let us now examine single-particle dynamics by using the initial **B** profile (Eq. (2)) as reference, focusing on electron dynamics which mainly govern flux ropes with scale lengths of $\sim d_i$. The normalized vector potential can be chosen to be $\bar{\mathbf{A}} = -\hat{z}\left[\ln\left(1+\bar{r}^2\right)\right]/2 + \hat{\phi} b_g \bar{r}/2$, where $\bar{\mathbf{A}} = \mathbf{A}/\lambda B_0$. Since the Lagrangian is $\bar{L} = \bar{v}^2/2 + \bar{\mathbf{v}} \cdot \bar{\mathbf{A}}$, we can find three conserved quantities, namely the canonical momentum in the z-direction $\bar{p}_z = \bar{v}_z + \bar{A}_z$, the canonical angular momentum $\bar{L}_\phi = \bar{r}\bar{v}_\phi + \bar{r}\bar{A}_\phi$, and the Hamiltonian $\bar{H} = \bar{v}^2/2 + \Phi$. Then, the normalized electron velocities are:

$$\bar{v}_z = \bar{p}_z + \frac{1}{2}\ln\left(1+\bar{r}^2\right), \tag{7}$$

$$\bar{v}_\phi = \frac{\bar{L}_\phi}{\bar{r}} - \frac{1}{2} b_g \bar{r}, \tag{8}$$

$$\bar{v}_r = \pm\sqrt{2\left(\bar{H}-\Phi\right) + v_\phi^2(\bar{r}) + v_z^2(\bar{r})}. \tag{9}$$

Note that the velocities are normalized by $\lambda\omega_{c\sigma}$ which includes the sign of the particle charge, so a positive normalized velocity contributes positively to the current density and vice versa.

Figure 4 shows the trajectory of a representative electron in the PIC simulation during its centripetal action from $t = 0$ to $60\omega_{\mathrm{pi}}^{-1}$. The red lines are the initial trajectories described by Eqs. (7)–(9). In Fig. 4a, the electron undergoes periodic motion in (r, v_r), and adiabatically travels toward $r = 0$ while approximately conserving its phase-space area. Thus, its oscillation in r decreases while its oscillation in v_r increases, resulting in heating in the r-direction.

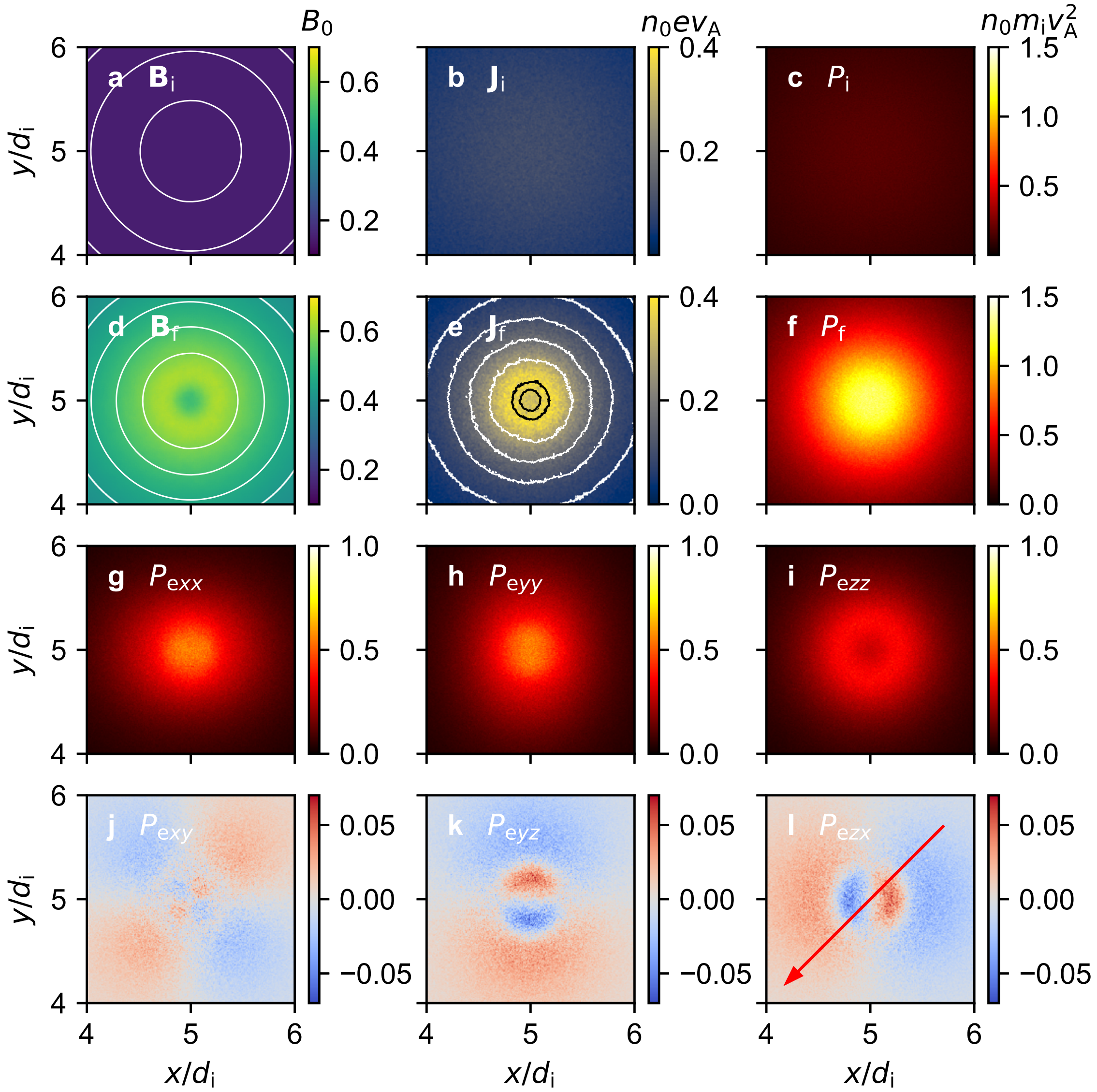

Fig. 3 | 2D profiles of various physical quantities. The initial **a** magnetic field **B**, **b** current density **J**, and **c** thermal pressure P and their final states (**d**–**f**). The units for **B**, **J**, and P are B_0, $n_0 e v_A$, and $n_0 m_i v_A^2$, respectively. Vector quantities are represented by their in-plane (lines; white for $+\phi$-direction and black for $-\phi$-direction) and out-of-plane (colors) components. Diagonal (**g**–**i**) and off-diagonal (**j**–**l**) components of the electron pressure tensor, again in units of $n_0 m_i v_A^2$.

In Fig. 4b, the electron initially follows the line predicted by Eq. (8) with $\bar{L}_\phi>0$ in (r, v_ϕ) space. As it travels toward $r = 0$, it accesses higher average $\bar{v}_\phi$ and so induces positive J_ϕ and also B_z. Its excursion in v_ϕ-space increases as well, indicating heating in the ϕ-direction. This, together with r-directed heating, results in increases in P_{exx} and P_{eyy} (Fig. 3). For axis-encircling particles which have $\bar{L}_\phi<0$ and thus negative $\bar{v}_\phi$ for all t, their traveling toward $r = 0$ decreases $\bar{v}_\phi$ and increases $-J_\phi$, corresponding to the $-\hat{\phi}$-directed current in Fig. 3e.

In Fig. 4c, the electron initially follows the line predicted by Eq. (7) in (r, v_z) space, which, because $\ln(1+\bar{r}^2) \simeq \bar{r}^2$ for small $\bar{r}$, is approximately a parabola with an intercept $\bar{p}_z$. As the system pinches and decreases in radial scale, so does the parabola while maintaining the intercept. As a result, $\bar{v}_z$ increases at finite r but less near $r = 0$ (think of a lotus flower shrugging its petals). This translates to the ring-like structure of J_z in Fig. 3e, which is in fact akin to bifurcated current sheets in Cartesian geometry[28]. The particle's excursion in $\bar{v}_z$ increases as well, i.e., z-directed heating. This heating, again, does not affect the region near $r = 0$, resulting in a dip in the P_{ezz} profile (Fig. 3i).

Although not explicitly discussed, the above analysis already includes the role of the electric fields. The electrostatic field E_r comes mainly from the Hall effect and the electron pressure gradient, i.e.:

$$\mathbf{E} = -\mathbf{u}_e \times \mathbf{B} - \frac{\nabla \cdot \mathbf{p}_e}{n_e e},$$

where $\mathbf{u}_e$, n_e, $\mathbf{p}_e$ are the electron fluid velocity, density, and pressure tensor, respectively. This electric field is manifested in Eq. (9) as Φ that affects the shape of the radial effective potential and thus the trajectory in $(\bar{r}, \bar{v}_r)$ space. This change in $\bar{r}$ oscillation in turn changes $\bar{v}_\phi$ and $\bar{v}_z$ through Eqs. (8) and (7). E_ϕ and E_z are the inductive components that change $\bar{A}_\phi$ and $\bar{A}_z$ which are the last terms in Eqs. (8) and (7). In the final state of the fiducial run, particle orbits are mainly magnetically-driven, i.e., $\mathbf{E} \times \mathbf{B}$ drifts are much less than magnetic (grad-B and curvature) drifts, because the Hall and pressure gradient terms nearly cancel each other out. Also, note that an initial Φ can be frame-transformed away as long as the vector potential has the same functional form over the domain of interest; this is what is done in the Harris solution[37].

These changes in phase-space trajectories change the phase-space distributions. Figure 5 shows the change in the electron distribution function Δf_e in different phase-spaces as the system reaches equilibrium. The

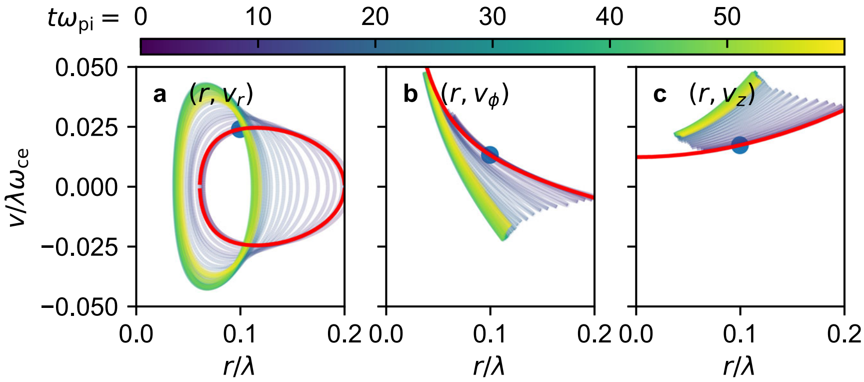

Fig. 4 | Electron phase-space trajectories. Trajectory of a representative electron in **a** (r, v_r), **b** (r, v_ϕ), **c** (r, v_z) spaces for $t = 0$ to $60\omega_{\rm pi}^{-1}$ (viridis color). The blue dot indicates the initial positions, and the red lines are the initial trajectories described by Eqs. (7)–(9).

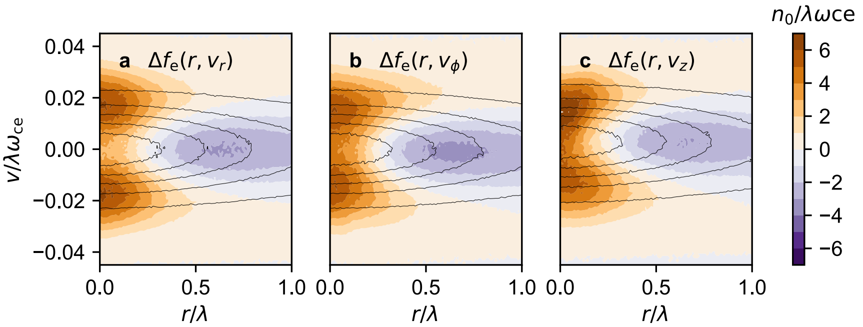

Fig. 5 | Electron distribution changes. Change in the electron distribution function $\Delta f_{\rm e}$ from $t = 0$ to $200\omega_{\rm pi}^{-1}$ in **a** (r, v_r), **b** (r, v_ϕ), and **c** (r, v_z) spaces. The black contours are $f_{\rm e}(t = 0)$. The distribution function is in units of $n_0/\lambda\omega_{\rm ce}$.

black contours are $f_{\rm e}$ at $t = 0$. The electrons migrate from the purple regions to the orange regions. In all spaces, $f_{\rm e}$ moves into regions of low r and high $|\bar{v}|$, i.e., the electron pressure increases. In Fig. 5b, $\Delta f_{\rm e}$ is asymmetric with respect to $\bar{v}_\phi = 0$ and is higher in the $+\bar{v}_\phi$ region; this translates to the increase of J_ϕ necessary to amplify B_z. In Fig. 5c, $\Delta f_{\rm e}$ is also asymmetric in such a way that the average $\bar{v}_z$ is higher around $\bar{r} \lesssim 0.2$ but lower at larger $r \gtrsim 0.2$, which leads to pinching of J_z. The final distribution function is far from Maxwellian and is determined by the allowed particle orbits for the given electromagnetic field. Also, the final current density profile is supported by a combination of the density and drift velocity profiles, in contrast to many kinetic equilibrium solutions in which it is supported entirely by the density profile with a spatially uniform drift velocity[30,37,38]. The former is a much more likely state if the source for particle acceleration is local rather than uniform.

Spacecraft comparison

We now present a Magnetospheric Multiscale (MMS) observation of an ion-scale flux rope that has formed and equilibrated through this pinching process. On July 6th 2017, when MMS was located at $\sim(-22.1, 3.1, 3.0)R_E$, it passed through an ion-scale flux rope traveling earthward with a reference frame velocity of $(811, -24, -61)$ km/s in geocentric solar magnetospheric (GSM) coordinates[26]. For a comparative analysis, another PIC simulation was conducted with parameters that are closer to the observed parameters. Namely, the mass ratio was set to $m_{\rm i}/m_{\rm e} = 400$, $v_{\rm A}/c = 0.025$, $b_{\rm g} = 0.3$, $t_{\rm max} = 500\omega_{pi}^{-1}$, and the direction of J_z was reversed to match the observed flux rope (initially $\mathbf{J}\cdot\mathbf{B} < 0$). The non-equilibrium dynamics of the rope and the eventual equilibrium are qualitatively similar to the fiducial run except for some sign changes.

A particular coordinate system was chosen to better compare the MMS observation to the PIC simulation (see Methods). Namely, coordinates of the same event obtained by Sun et al.[26] through a combination of the spatio-temporal difference (STD) and minimum directional derivative (MDD) methods were redefined so that our z-axis is the out-of-plane direction and rotated about the z-axis by $7\pi/8$. The resultant unit vectors in GSM coordinates are $\vec{x} = [-0.361, -0.22, -0.9]$, $\vec{y} = [0.889, 0.222, -0.409]$, and $\vec{z} = [0.291, -0.950, 0.116]$.

Figure 6a–e shows the observed profiles of **B, J**$_{\rm e}$, $n_{\rm e}$, and all six components of the electron temperature tensor. **J** was calculated after subtracting the reference frame velocity of the flux rope. Figure 6f–j shows the synthetic profiles from the PIC simulation, obtained by taking a cut in the direction of the red arrow in Fig. 3l. The length scale of the observed flux rope is around ~1000 km[26] which is $\sim 2d_{\rm i}$, comparable to the simulated flux rope.

There is good agreement between the two flux ropes in all properties. A distinctly striking agreement is among all six components of the electron temperature tensor. In particular, the diagonal components are well explained by double-adiabatic closures, but non-equilibrium dynamics and particle phase-space distributions must be invoked to explain the off-diagonal components. Although the agreement on T_{exy} is weaker than other components, the magnetic field profile of the observed flux rope agrees less with the simulation flux rope on the left side of the origin ($l < 0$), so the slight disagreement of T_{exy} can be accounted for. The overall comparison well substantiates the claim that the observed flux rope has formed from this pinching process.

Discussion

An important implication of this model is that flux rope formation through current pinching dynamics must involve non-ideal-MHD dynamics or boundaries. This is because finite $\mathbf{J}\cdot\mathbf{B}$ is necessary to initiate the pinching process, but $\mathbf{E}\cdot\mathbf{B} = 0$ in ideal MHD so parallel current drive is not possible. Thus, the initial condition must have been induced by non-MHD processes, although subsequent dynamics may be MHD. This aligns with many flux rope formation models which involve non-MHD processes such as magnetic reconnection and kinetic turbulence[31–34], and also with generic laboratory methods of flux rope generation by helicity injection at the boundaries[6,8]. Guide-field reconnection, which is a well-known source of flux ropes[31], generates a parallel reconnection electric field that induces parallel current. Kinetic turbulence heavily involves reconnection as well.

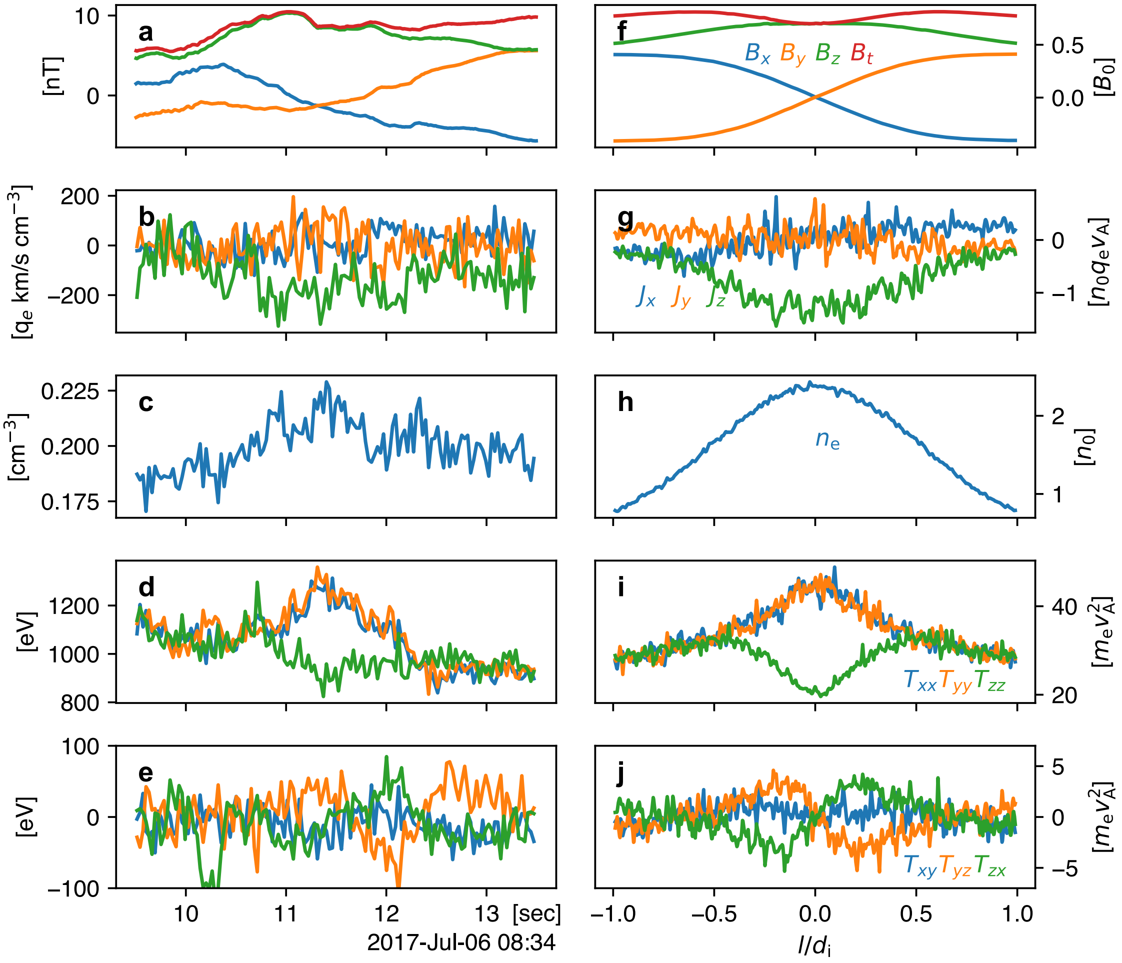

Fig. 6 | Comparisons to spacecraft observations. MMS spacecraft crossing of a flux rope on July 6th 2017, compared to a synthetic crossing from the PIC simulation. Observed profiles of **a** the magnetic field **B**, and **b** electron current density $\mathbf{J}_e$. The x, y, and z components correspond to the blue, orange, and green lines, respectively. The total magnetic field |**B**| is represented by the red line. Observed profiles of the **c** electron density n_e, **d** diagonal components and **e** off-diagonal components of the electron temperature tensor. Again, each component of the pressure tensor is differentiated by the blue, orange, and green colors. **f**–**j** Corresponding profiles from the PIC simulation. **J** was calculated after subtracting the reference frame velocity of the flux rope. The velocity of the spacecraft was ~800 km s^{-1}, and so the length scale of the observed flux rope was ~1000 km s^{-1}, which is ~2d_i, comparable to the simulated flux rope.

Helicity injection in laboratory flux ropes is typically achieved by voltage sources combined with bias magnetic fields, which induce parallel electric fields and current. Kinetic instabilities are also known to serve as a localized load impedance that can generate parallel electric fields[19,39].

Another important implication of this model is that small-scale flux ropes can form from larger-scale initial conditions via pinching. If the initial plasma beta and guide field strengths are sufficiently weak or, equivalently, the initial parallel current is sufficiently strong, it is possible to transition from MHD scales to kinetic scales. This process enables non-adiabatic and agyrotropic particle motions and kinetic instabilities, which have recently proven to be crucial for instigating solar eruptions[19].

As discussed above, the eventual flux rope profile depends heavily on the initial conditions at which the parallel current was induced. Thus, non-equilibrium dynamics and phase-space distributions must be taken into account to come up with good kinetic flux rope models. In particular, the observed temperature tensor profiles in Fig. 6 cannot be explained without invoking kinetic pinching dynamics. However, for lack of better solutions, Grad–Shafranov models that use only scalar pressure are readily used to reconstruct 2D flux rope structure from line measurements[11,26,34]; an improved model that takes into account the variation in the pressure tensor due to non-equilibrium dynamics is thus exigent.

Our present model focuses on kinetic-scale flux ropes. However, even for flux ropes, e.g., in solar environments, whose time and length scales are relatively slower and larger, the pressure tensor may become anisotropic due to non-equilibrium dynamics and frozen-in flux. For sufficiently high-beta situations, this anisotropy may place limits on stable flux rope configurations due to mirror/firehose instabilities[40,41], which will be further investigated.

Although the initial conditions of our model are superficially simple, the ensuing non-equilibrium dynamics and the eventual equilibrium attained is rather complicated yet can still be explained in simple terms through particle orbits. Nonetheless, there are some restrictions of the model that need to be addressed. First, we assume a 2D geometry, which corresponds to a situation where the curvature of the flux rope axis is much larger than its radius. If the two length scales are comparable, models akin to Taylor states should be developed. Also, the 2D assumption means that the model cannot address dynamics such as the torus instability[16], although some 3D processes like kink and sausage instabilities can be addressed by calculating the Kruskal–Shafranov criterion in the final equilibrium state. Second, our model obviously falls short of explaining highly collisional systems, although they can be regarded to some degree as special cases of the present model with isotropic scalar pressure.

In conclusion, we have investigated the dynamics of a kinetic-scale flux rope from its non-equilibrium formation to relaxation. It was shown that a localized current parallel to the background magnetic field is a sufficient condition for flux rope generation via pinching. By comparing spacecraft observation to PIC simulations, a representative flux rope observed by MMS was shown to be consistent with generation by this very process, and its structure was explicable down to all components of the electron temperature tensor. Several implications of this model were discussed, namely its initially non-MHD nature, connection between MHD and kinetic scales, and a need for better kinetic flux rope models that can accommodate deviations from isotropic pressure tensors.

Methods

Vlasov calculation

The normalized Vlasov equation for an initially zero electric field is:

$$\frac{\partial f_\sigma}{\partial \bar{t}} + \bar{\mathbf{v}} \cdot \frac{\partial f_\sigma}{\partial \bar{\mathbf{r}}} + \left(\bar{\mathbf{v}} \times \bar{\mathbf{B}}\right) \cdot \frac{\partial f_\sigma}{\partial \bar{\mathbf{v}}} = 0, \tag{10}$$

where barred quantities are normalized. Equation (1) gives:

$$\frac{\partial f_\sigma}{\partial \bar{\mathbf{r}}} = \frac{-4\bar{r} f_\sigma}{1+\bar{r}^2}\hat{r}, \tag{11}$$

$$\frac{\partial f_\sigma}{\partial \bar{\mathbf{v}}} = \frac{-(\bar{\mathbf{v}} - \bar{V}_\sigma \hat{z}) f_\sigma}{\bar{v}_{\mathrm{T}\sigma}^2}, \tag{12}$$

and so Eq. (10) becomes:

$$\frac{\partial f_\sigma}{\partial \bar{t}} - \frac{4\bar{r} f_\sigma}{1+\bar{r}^2}\bar{v}_r + \left(\bar{\mathbf{v}} \times \bar{\mathbf{B}}\right) \cdot \hat{z}\frac{\bar{V}_\sigma f_\sigma}{\bar{v}_{\mathrm{T}\sigma}^2} = 0. \tag{13}$$

Inserting Eq. (2):

$$\frac{\partial f_\sigma}{\partial \bar{t}} - \frac{4\bar{r} f_\sigma}{1+\bar{r}^2}\bar{v}_r + \bar{v}_r \frac{\bar{r}}{1+\bar{r}^2}\frac{\bar{V}_\sigma f_\sigma}{\bar{v}_{\mathrm{T}\sigma}^2} = 0, \tag{14}$$

$$\frac{\partial f_\sigma}{\partial \bar{t}} + \frac{4\bar{r} f_\sigma}{1+\bar{r}^2}\bar{v}_r \left(\frac{\bar{V}_\sigma}{4\bar{v}_{\mathrm{T}\sigma}^2} - 1\right) = 0, \tag{15}$$

which yields Eq. (4).

For a small time interval $\delta\bar{t}$, Eq. (4) can be solved as, writing $\xi = \bar{V}_\sigma / 4\bar{v}_{\mathrm{T}\sigma}^2 - 1$:

$$\begin{aligned}
\ln\left(\frac{f_\sigma(\bar{t} = \delta\bar{t})}{f_\sigma(\bar{t} = 0)}\right) &= -\,\bar{v}_r \frac{4\bar{r}\xi\delta\bar{t}}{1+\bar{r}^2}, \\
f_\sigma(\bar{t} = \delta\bar{t}) &= \left(\frac{1}{2\pi v_{\mathrm{T}\sigma}^2}\right)^{3/2} \exp\left(-\frac{\left(\bar{\mathbf{v}} - \bar{V}_\sigma \hat{z}\right)^2}{2\bar{v}_{\mathrm{T}\sigma}^2} - \bar{v}_r \frac{4\bar{r}\xi\delta\bar{t}}{1+\bar{r}^2}\right)\frac{n_0}{(1+\bar{r}^2)^2}, \\
&= \left(\frac{1}{2\pi v_{\mathrm{T}\sigma}^2}\right)^{3/2} \exp\left(-\frac{\left(\bar{\mathbf{v}} - \bar{V}_{r\sigma}\hat{r} - \bar{V}_\sigma \hat{z}\right)^2}{2\bar{v}_{\mathrm{T}\sigma}^2} + \mathcal{O}\left(\delta\bar{t}^2\right)\right)\frac{n_0}{(1+\bar{r}^2)^2},
\end{aligned}$$

which corresponds to Eqs. (5) and (6).

Particle-in-cell simulation

The open-source, fully-relativistic particle-in-cell code, SMILEI[42], was used. The simulation domain was $L_x \times L_y = 10d_\mathrm{i} \times 10d_\mathrm{i}$ on a 1024×1024 grid. The electromagnetic field boundary condition was Silver-Müller. The particle boundary condition was set to remove on exit, and a thermal plasma was continuously injected to replenish the lost particles. A total of 100–200 particles per cell were placed depending on the initial local density. The fiducial run was conducted with a mass ratio $m_i/m_e = 100$, Alfven velocity $v_A/c = 0.1$, initial guide field $b_\mathrm{g} = 0.15$, total time $200\omega_{\mathrm{pi}}^{-1}$, and timestep $\Delta t = 6.56 \times 10^{-3}\omega_{\mathrm{pi}}^{-1}$. The run that was compared with spacecraft observations was conducted with $m_\mathrm{i}/m_\mathrm{e} = 400$, $v_\mathrm{A}/c = 0.025$, $b_\mathrm{g} = 0.3$, and total time $500\omega_{\mathrm{pi}}^{-1}$.

MMS data and coordinate system

MMS1 data from 08:23:09.5 to 08:23:13.5 UT on 6 July 2017 were used to yield the profile in Fig. 6a–e. The data were imported using the pySPEDAS package[43]. The magnetic field data and plasma data were collected by the Fluxgate Magnetometer instrument[44] and the Fast Plasma Investigation instrument[45], respectively.

A particular coordinate system was constructed for a better comparison with the simulation results. We first took the XYZ coordinates calculated by Sun et al.[26], namely $X = [-0.96, -0.29, 0.03]$, $Y = [0.291, -0.95, 0.12]$, $Z = [-0.0042, 0.12, 0.99]$ in GSM coordinates, and redefined Y to be our z-axis—the out-of-plane direction—by shuffling (X, Y, Z) to (Z, X, Y). The well-known Rodrigues' rotation formula was used to rotation the coordinates about the z-axis by $7\pi/8$. The resultant unit vectors in GSM coordinates are $\overrightarrow{x} = [-0.361, -0.22, -0.9]$, $\overrightarrow{y} = [0.889, 0.222, -0.409]$, and $\overrightarrow{z} = [0.291, -0.950, 0.116]$.

Data availability

MMS data are publicly available from https://lasp.colorado.edu/mms/sdc/public. PIC simulation data for the fiducial run are available from https://doi.org/10.5281/zenodo.12191434. PIC simulation data for the MMS comparison are available from the corresponding author upon reasonable request.

Code availability

SMILEI[42] is an open-source particle-in-cell code available from https://smileipic.github.io/Smilei. MMS data were imported and analyzed using the pySPEDAS package[43], available from https://github.com/spedas/pyspedas. The codes used in data analysis and figure generation are available at https://github.com/ydyoon93/FluxRopeFormationPostProcess.git.

Received: 25 July 2024; Accepted: 19 August 2024;
Published online: 03 September 2024

References

1. Russell, C., Priest, E. & Lee, L. *Physics of Magnetic Flux Ropes* (American Geophysical Union, 1990).
2. Babcock, H. W. The topology of the sun's magnetic field and the 22-year cycle. *Astrophys. J.* **133**, 572 (1961).
3. Schmieder, B., Raadu, M. & Malherbe, J. Twisting motions in a disturbed solar filament. *Astron. Astrophys.* **142**, 249–255 (1985).
4. Slavin, J. A. et al. Geotail observations of magnetic flux ropes in the plasma sheet. *J. Geophys. Res. Space Phys.* **108**, 1015 (2003).
5. Goldstein, H. On the field configuration in magnetic clouds. In *JPL Solar Wind Five* Vol. 2280, p. 731 (NASA Conference Publ, 1983).
6. Lawrence, E. E. & Gekelman, W. Identification of a quasiseparatrix layer in a reconnecting laboratory magnetoplasma. *Phys. Rev. Lett.* **103**, 105002 (2009).
7. Bellan, P. M. & Hansen, J. F. Laboratory simulations of solar prominence eruptions. *Phys. Plasmas* **5**, 1991–2000 (1998).
8. Hansen, J. F., Tripathi, S. K. & Bellan, P. M. Co- and counter-helicity interaction between two adjacent laboratory prominences. *Phys. Plasmas* **11**, 3177–3185 (2004).
9. Tripathi, S. K. P., Bellan, P. M. & Yun, G. S. Observation of kinetic plasma jets in a coronal-loop simulation experiment. *Phys. Rev. Lett.* **98**, 135002 (2007).
10. Moldwin, M. B., Ford, S., Lepping, R., Slavin, J. & Szabo, A. Small-scale magnetic flux ropes in the solar wind. *Geophys. Res. Lett.* **27**, 57–60 (2000).
11. Chen, Y. et al. Small-scale magnetic flux ropes in the first two parker solar probe encounters. *Astrophys. J.* **903**, 76 (2020).
12. Kivelson, M. G. & Khurana, K. K. Models of flux ropes embedded in a harris neutral sheet: force-free solutions in low and high beta plasmas. *J. Geophys. Res. Space Phys.* **100**, 23637–23645 (1995).

13. Karimabadi, H., Krauss-Varban, D., Omidi, N. & Vu, H. X. Magnetic structure of the reconnection layer and core field generation in plasmoids. *J. Geophys. Res. Space Phys.* **104**, 12313–12326 (1999).
14. Russell, C. T. et al. Structure, force balance, and topology of earth's magnetopause. *Science* **356**, 960–963 (2017).
15. Intrator, T. P., Sun, X., Lapenta, G., Dorf, L. & Furno, I. Experimental onset threshold and magnetic pressure pile-up for 3d reconnection. *Nat. Phys.* **5**, 521–526 (2009).
16. Kliem, B. & Torok, T. Torus instability. *Phys. Rev. Lett.* **96**, 255002 (2006).
17. Russell, C. T. & Elphic, R. C. Initial isee magnetometer results: magnetopause observations. *Space Sci. Rev.* **22**, 681–715 (1978).
18. DeHass, T. *Transformation of Canonical Helicity Under the Collision and Merging of Two Magnetic Flux Ropes*. PhD Thesis (UCLA, 2017).
19. Zhang, Y., Pree, S. & Bellan, P. M. Generation of laboratory nanoflares from multiple braided plasma loops. *Nat. Astron.* **7**, 655–661 (2023).
20. Gold, T. & Hoyle, F. On the origin of solar flares. *Mon. Not. R. Astron. Soc.* **120**, 89–105 (1960).
21. Burlaga, L. F. Magnetic clouds and force-free fields with constant alpha. *J. Geophys. Res. Space Phys.* **93**, 7217–7224 (1988).
22. Lepping, R. P., Jones, J. A. & Burlaga, L. F. Magnetic field structure of interplanetary magnetic clouds at 1 au. *J. Geophys. Res. Space Phys.* **95**, 11957–11965 (1990).
23. Hidalgo, M. A. A study of the expansion and distortion of the cross section of magnetic clouds in the interplanetary medium. *J. Geophys. Res* **108**, 1320 (2003).
24. Nieves-Chinchilla, T. et al. A circular-cylindrical flux-rope analytical model for magnetic clouds. *Astrophys. J.* **823**, 27 (2016).
25. Nieves-Chinchilla, T., Linton, M. G., Hidalgo, M. A. & Vourlidas, A. Elliptic-cylindrical analytical flux rope model for magnetic clouds. *Astrophys. J.* **861**, 139 (2018).
26. Sun, W. J. et al. Mms study of the structure of ion-scale flux ropes in the earth's cross-tail current sheet. *Geophys. Res. Lett.* **46**, 6168–6177 (2019).
27. Nieves-Chinchilla, T. et al. Redefining flux ropes in heliophysics. *Front. Astron. Space Sci.* **10** https://www.frontiersin.org/articles/10.3389/fspas.2023.1114838/full (2023).
28. Yoon, Y. D., Yun, G. S., Wendel, D. E. & Burch, J. L. Collisionless relaxation of a disequilibrated current sheet and implications for bifurcated structures. *Nat. Commun.* **12**, 3774 (2021).
29. Yoon, Y. D., Wendel, D. E. & Yun, G. S. Equilibrium selection via current sheet relaxation and guide field amplification. *Nat. Commun.* **14**, 139 (2023).
30. Bennett, W. H. Magnetically self-focussing streams. *Phys. Rev.* **45**, 890–897 (1934).
31. Daughton, W. et al. Role of electron physics in the development of turbulent magnetic reconnection in collisionless plasmas. *Nat. Phys.* **7**, 539–542 (2011).
32. Oieroset, M. et al. Direct evidence for a three-dimensional magnetic flux rope flanked by two active magnetic reconnection x lines at earth's magnetopause. *Phys. Rev. Lett.* **107**, 165007 (2011).
33. Eastwood, J. P. et al. Ion-scale secondary flux ropes generated by magnetopause reconnection as resolved by mms. *Geophys. Res. Lett.* **43**, 4716–4724 (2016).
34. Zheng, J. & Hu, Q. Observational evidence for self-generation of small-scale magnetic flux ropes from intermittent solar wind turbulence. *Astrophys. J. Lett.* **852**, L23 (2018).
35. Myers, C. E. et al. A dynamic magnetic tension force as the cause of failed solar eruptions. *Nature* **528**, 526–529 (2015).
36. Yun, G. S. et al. Appearance and dynamics of helical flux tubes under electron cyclotron resonance heating in the core of kstar plasmas. *Phys. Rev. Lett.* **109**, 145003 (2012).
37. Harris, E. G. On a plasma sheath separating regions of oppositely directed magnetic field. *Il Nuovo Cimento* **23**, 115–121 (1962).
38. Yoon, P. H. & Lui, A. T. Y. Model of ion- or electron-dominated current sheet. *J. Geophys. Res. Space Phys.* **109**, 11213 (2004).
39. Moser, A. L. & Bellan, P. M. Magnetic reconnection from a multiscale instability cascade. *Nature* **482**, 379–381 (2012).
40. Kunz, M., Schekochihin, A. & Stone, J. Firehose and mirror instabilities in a collisionless shearing plasma. *Phys. Rev. Lett.* **112**, 205003 (2014).
41. Squire, J., Kunz, M., Quataert, E. & Schekochihin, A. Kinetic simulations of the interruption of large-amplitude shear-alfvén waves in a high-beta plasma. *Phys. Rev. Lett.* **119**, 155101 (2017).
42. Derouillat, J. et al. Smilei: a collaborative, open-source, multi-purpose particle-in-cell code for plasma simulation. *Comput. Phys. Commun.* **222**, 351–373 (2018).
43. Angelopoulos, V. et al. The space physics environment data analysis system (spedas). *Space Sci. Rev.* **215**, 9 (2019).
44. Torbert, R. B. et al. The fields instrument suite on mms: scientific objectives, measurements, and data products. *Space Sci. Rev.* **199**, 105–135 (2016).
45. Pollock, C. et al. Fast plasma investigation for magnetospheric multiscale. *Space Sci. Rev.* **199**, 331–406 (2016).

Acknowledgements

The authors thank Kyunghwan Dokgo for useful discussions. This work was supported by an appointment to the JRG Program at the APCTP through the Science and Technology Promotion Fund and Lottery Fund of the Korean government, and also by the Korean Local Governments—Gyeongsangbuk-do Province and Pohang City. This work was also supported by the National Research Foundation of Korea under Grant No. RS-2023-00281272. T.E.M. was supported by the NASA Magnetospheric Multiscale Mission Project and Science Team under Contract #80GSFC17C003. The computations presented here were conducted on the KAIROS supercomputing cluster at the Korean Institute of Fusion Energy, and on the APCTP computing server.

Author contributions

Y.D.Y. conceived the project, performed the simulations and spacecraft data processing, and wrote the manuscript. G.S.Y., T.E.M. and M.L. contributed to discussion of the material, interpretation of data, and revision of the manuscript.

Competing interests

The authors declare no competing interests.

Additional information

Supplementary information The online version contains supplementary material available at https://doi.org/10.1038/s42005-024-01784-6.

Correspondence and requests for materials should be addressed to Young Dae Yoon.

Peer review information *Communications Physics* thanks the anonymous reviewers for their contribution to the peer review of this work. A peer review file is available.

Reprints and permissions information is available at http://www.nature.com/reprints

Publisher's note Springer Nature remains neutral with regard to jurisdictional claims in published maps and institutional affiliations.

Open Access This article is licensed under a Creative Commons Attribution-NonCommercial-NoDerivatives 4.0 International License, which permits any non-commercial use, sharing, distribution and reproduction in any medium or format, as long as you give appropriate credit to the original author(s) and the source, provide a link to the Creative Commons licence, and indicate if you modified the licensed material. You do not have permission under this licence to share adapted material derived from this article or parts of it. The images or other third party material in this article are included in the article's Creative Commons licence, unless indicated otherwise in a credit line to the material. If material is not included in the article's Creative Commons licence and your intended use is not permitted by statutory regulation or exceeds the permitted use, you will need to obtain permission directly from the copyright holder. To view a copy of this licence, visit http://creativecommons.org/licenses/by-nc-nd/4.0/.

© The Author(s) 2024